Monthly Notices of the ROYAL ASTRONOMICAL SOCIETY

MNRAS **502,** 1694–1701 (2021) doi:10.1093/mnras/staa4003
Advance Access publication 2021 January 4

SN 2014C: VLBI image shows a shell structure and decelerated expansion

Michael F. Bietenholz [1,2]★ Norbert Bartel,[1] Atish Kamble,[3] Raffaella Margutti,[4]‡
David Jacob Matthews[4] and Danny Milisavljevic[5]

[1]*Department of Physics and Astronomy, York University, Toronto, ON M3J 1P3, Canada*
[2]*SARAO/Hartebeesthoek Radio Observatory, PO Box 443, Krugersdorp 1740, South Africa*
[3]*Harvard-Smithsonian Center for Astrophysics, 156 Madison Ave, Arlington, MA 02474, USA*
[4]*Center for Interdisciplinary Exploration and Research in Astrophysics (CIERA) and Department of Physics and Astronomy, Northwestern University, Evanston, IL 60208, USA*
[5]*Department of Physics and Astronomy, Purdue University, 525 Northwestern Ave., West Lafayette, IN 47907, USA*

Accepted 2020 December 17. Received 2020 November 19; in original form 2020 September 24

ABSTRACT

We report on new Very Long Baseline Interferometry radio measurements of supernova (SN) 2014C in the spiral galaxy NGC 7331, made with the European VLBI Network ∼5 yr after the explosion, as well as on flux density measurements made with the Jansky Very Large Array (VLA). SN 2014C was an unusual SN, initially of Type Ib, but over the course of ∼1 yr, it developed strong Hα lines, implying the onset of strong interaction with some H-rich circumstellar medium (CSM). The expanding shock-front interacted with a dense shell of circumstellar material during the first year, but has now emerged from the dense shell and is expanding into the lower density CSM beyond. Our new VLBI observations show a relatively clear shell structure and continued expansion with some deceleration, with a suggestion that the deceleration is increasing at the latest times. Our multifrequency VLA observations show a relatively flat power-law spectrum with $S_\nu \propto \nu^{-0.56 \pm 0.03}$, and show no decline in the radio luminosity since $t \sim 1$ yr.

Key words: Supernovae: individual: SN 2014C – radio continuum: general .

1 INTRODUCTION

Supernova (SN) 2014C was a very unusual SN, and its progenitor had complex mass-loss in the time before the explosion. SN 2014C was discovered on 2014 January 5 in the nearby early-type spiral galaxy NGC 7331 by the Lick Observatory Supernova Search (Kim et al. 2014). We adopt the updated Cepheid distance of $D = 15.1 \pm 0.7$ Mpc from Saha et al. (2006),[1] and an explosion date, $t = 0$, of 2013 December 30.0 (UT) = MJD 56656.0, as determined by Margutti et al. (2017) from bolometric light-curve modelling.[2]

At its discovery, SN 2014C had the spectrum of ordinary, H-stripped Type Ib supernova (SN Ib; Kim et al. 2014; Tartaglia et al. 2014). Unfortunately, no spectra could be obtained for several months thereafter as it went behind the sun, but after it emerged, the spectrum had evolved into an SN IIn one, with prominent Hα lines, which implied strong interaction with the circumstellar medium (CSM) (Milisavljevic et al. 2015; Margutti et al. 2017). At $t = 20$ d, it was faint in X-rays, but, unusually, rose till $t \sim 1$ yr and has remained high since (Margutti et al. 2017; Jin & Kong 2019). In the mid-infrared, it had a high and almost constant brightness till $t \sim 5.5$ yr (Tinyanont et al. 2019).

SN 2014C was quickly also detected in the radio, at frequencies ranging from 7 to 85 GHz (Kamble et al. 2014; Zauderer et al. 2014). In the first month, it did not have a high radio luminosity ($L_\nu \sim 10^{26}$ erg s^{-1} Hz^{-1} at 7 GHz; Kamble et al. 2014). However, the luminosity rose rapidly after about one month, and then again around 1 yr (Anderson et al. 2017), and has stayed high. Due to its relative nearness and high radio brightness, it was a target for Very Long Baseline Interferometry (VLBI) observations. In Bietenholz et al. (2018), which we will refer to as Paper I hereafter, we presented our first four epochs of VLBI observations, between $t = 1.1$ and 2.9 yr, which showed that SN 2014C's forward shock was expanding at $v \simeq 13\,600$ km s^{-1} over that period, but must have been expanding more rapidly at $t < 1$ yr.

The picture of SN 2014C that has emerged (e.g. Milisavljevic et al. 2015; Margutti et al. 2017) is that the SN exploded as an SN Ib, with the progenitor having aleady lost most of its H envelope, inside a low-density cavity. Due to the low density, there was relatively little radio or X-ray emission initially. As the shock moved outward, at $t \sim 0.3$ yr, it encountered a shell of very dense circumstellar material (CSM), causing emission at both X-rays and radio to brighten. Interaction with the CSM commonly produces both radio and X-ray emission (e.g. Chevalier & Fransson 2017).

The shell was formed due to a mass ejection event shortly before the SN explosion. The shock has since progressed through this

★ E-mail: mbieten@yorku.ca
‡ CIFAR Azrieli Global Scholar, Gravity & the Extreme Universe Program, 2019.

[1]The NASA/IPAC Extragalactic Database (NED; https://ned.ipac.caltech.edu) lists 54 redshift-independent distances, with mean and standard deviation 13.4 ± 2.7 Mpc. NED is funded by the National Aeronautics and Space Administration and operated by the California Institute of Technology.

[2]Although SN 2014C's explosion date is not tightly constrained, it is uncertain by less than one week, and the exact value will have little effect on our results which are at times several years after the explosion. The NASA/IPAC Extragalactic Database (NED) is funded by the National Aeronautics and Space Administration and operated by the California Institute of Technology.

overdense shell, and is currently expanding through the moderately dense wind of the progenitor from the time before the ejection event.

In the few cases, like SN 2014C, where an SN is near enough to be resolved with VLBI observations, they can provide crucial direct observational constraints on basic physical parameters of the SN, in particular the (time-dependent) radius of the expanding ejecta and the corresponding expansion speed. In Paper I, we used VLBI observations to determine the radius, r, of the shock in SN 2014C at various epochs, and found a radius of $r_{16} = 14.4 \pm 0.6$, at $t = 2.9$ yr, where r_{16} is a dimensionless radius, and is equal to $r/(10^{16}$ cm).

In order to continue to study the evolution of SN 2014C, we made new VLBI observations, this time with the European VLBI Network (EVN), ∼2 yr after those presented in Paper I. Our new image has the highest resolution relative to the shell size for this SN to date. We also report on observations with the Karl G. Jansky Very Large Array of the National Radio Astronomy Observatory (NRAO) in the USA to measure the total flux density and spectral energy distribution (SED) in early 2020.

2 OBSERVATIONS AND DATA REDUCTION

2.1 VLBI observations

We observed SN 2014C using the EVN on 2018 October 30 and 31 at 8.4 GHz (observing codes EB066A, EB066B). Both observations used a standard 1-Gbps experiment setup (eight subbands, 16-MHz bandwidth per subband, dual circular polarization, two-bit quantization). The participating telescopes were Westerbork (Wb, phased-array), Effelsberg (Ef), Medicina (Mc), Onsala(O6), Tianma (T6), Urumqi (Ur), Yebes (Ys), Hartebeesthoek (Hh) Svetloe (Sv), Zelenchukskaya (Zc), Badary (Bd), and Irbene (Ir). The correlation was done by the EVN software correlator (SFXC; Keimpema et al. 2015) at JIVE (Joint Institute for VLBI, ERIC) using standard correlation parameters of continuum experiments. Each of the two runs was 8 h in length.

We phase-referenced our observations to the source VCS1 J2248+3718, which we will refer to as just J2248+3718, and which is 2.°9 away from SN 2014C on the sky. We found it to be only marginally resolved.[3] We show the image of J2248+3718 in Fig. 1. Our phase-referencing calibration for SN 2014C, which provided the starting point for the phase self-calibration of SN 2014C, was based on the CLEAN model of J2248+3718.

The data reduction was carried out with NRAO's Astronomical Image Processing System (AIPS). The initial flux density calibration was done through measurements of the system temperature at each telescope, and improved through self-calibration of the phase-reference sources.

The signal-to-noise ratio on SN 2014C was high enough to permit self-calibration in phase. We started with self-calibrating the antennas T6, Bd, and Ir, which showed the most obvious failures in phase-referencing and exhibited phase-wrapping, due in part to inaccurate antenna positions. We used a 15-min solution interval, and an initial clean model made *excluding* the data from those three antennas. We then proceeded to include those three antennas in the imaging and the other antennas in the self-calibration, with a longer solution interval of 2 h, but overlapped so that we obtained a solution every hour. Both imaging and model-fitting results for SN 2014C are derived from the phase self-calibrated data.

[3]In Paper I, we had used the nearer NVSS J223555+341837 as a phase-reference source, but we found it to be significantly resolved, and we therefore switched to the less-resolved J2248+3718 for these observations. Since we were able to phase self-calibrate SN 2014C at 8.4 GHz both in this work and in Paper I, any structure in reference sources should not affect our results.

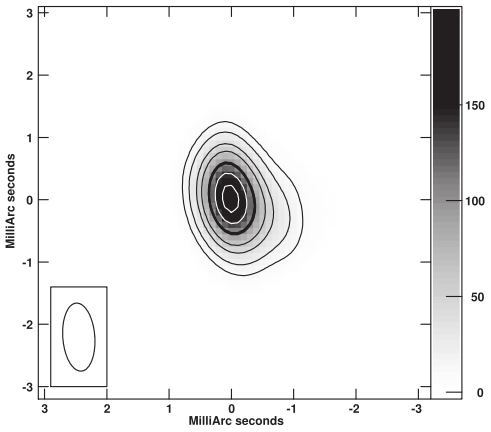

Figure 1. The VLBI image our phase-reference source J2248+3718. The contours are drawn at 5, 10, 20, 30, **50** (emphasized), 70, and 90 per cent of the peak brightness of 198 mJy beam^{-1}. The full width at half-maximum (FWHM) resolution of (1.09 × 0.51) mas at p.a. 4° is indicated at lower left. North is up and east is to the left.

2.2 VLA observations

We observed SN 2014C also with the VLA on 2020 May 6 (observing code 20A-441). The total length of the observing run was 2 h, and we observed at frequencies between 2 and 20 GHz. The data were reduced following standard procedures using the Common Astronomy Software Application (CASA; McMullin et al. 2007), with the flux density scale set by observations of 3C 286. The SN 2014C data were self-calibrated in phase only.

We measured flux densities by fitting an elliptical Gaussian of the same dimension as the restoring (clean) beam to the image, with a zero-level also being fit in cases where there was significant background emission from the galaxy, although in all cases, the galaxy background was less than the uncertainties. Our uncertainties include the statistical contribution due to the noise in the images, but are dominated by the 5 per cent uncertainty in the flux-density calibration at the VLA.

3 RESULTS

3.1 VLBI image

We show the VLBI image of SN 2014C, obtained on 2018 October 31, or $t = 4.8$ yr, in Fig. 2. The image was deconvolved using the clean algorithm, with AIPS robustness parameter set to +0.5. To increase the reliability of the images, we used the square root of the data weights in the imaging, which results in more robust images less dominated by a small number of very sensitive baselines. We also use the multiscale extension of the original clean algorithm, ms-clean (Wakker & Schwarz 1988), which produces superior results for extended sources see, e.g. Rich et al. 2008; Bietenholz et al. 2010b; Hunter et al. 2012). The total cleaned flux density was 15.8 mJy, the rms background brightness was 51 μJy beam^{-1}, and the FWHM resolution was (1.17 × 0.54) mas at p.a. 5°.

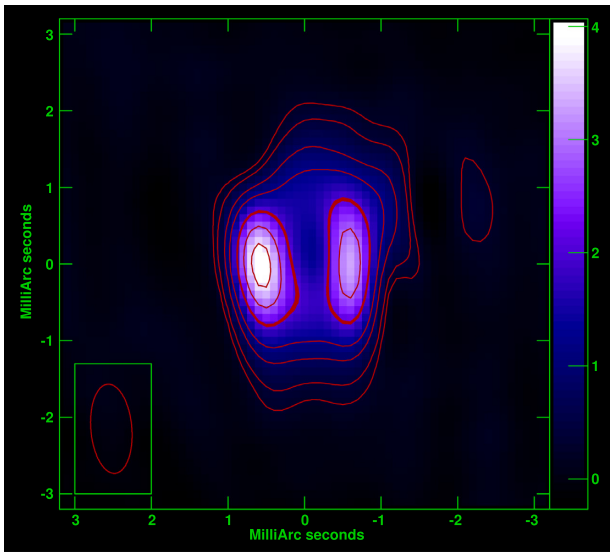

Figure 2. The VLBI image of SN 2014C on 2018 October 31 at $t = 4.8$ yr. Both the contours and colourscale show the brightness, the latter labelled in mJy beam^{-1}. The contours are at -6, 6, 10, 30, **50** (emphasized), 70, and 90 per cent of the image peak brightness of 4080 μJy beam^{-1}. The rms background brightness was 51 μJy beam^{-1}. The FWHM resolution of (1.17 × 0.54) mas at p.a. 5° is indicated at lower left. North is up and east is to the left.

The image shows a structure that is at least approximately circular in outline, with enhancement to the east and west, with the one in the east being about 25 per cent brighter. An east–west asymmetry of similar magnitude was seen in our image from $t = 2.9$ yr in Paper I, but in the opposite sense, with the west side being brighter. Such one-sided asymmetries in the radio brightness seem to be common in SNe (Bietenholz 2014; Bartel, Karimi & Bietenholz 2017), and they can vary with time (e.g. SN 1993J; Bietenholz, Bartel & Rupen 2003), but their origin is not known.

Is the enhancement in brightness to the east and west real, or is it merely due to the convolution of a circular ring-like brightness pattern with a north–south elongated restoring beam? To answer this question, we simulated visibility measurements for a source with complete circular symmetry, which simulated visibilities had the same elongated u–v coverage, and thus the same elongated restoring beam as our EVN observations. We added random Gaussian noise the simulated visibilities, scaled so as to produce the same image background rms as was found in the image made from the real data. We then deconvolved these simulated visibilities in the same fashion as the real data. Our source model was the projection of a spherical shell of emission, with a ratio of outer to inner radius, $\mathcal{R}_{\rm o/i} = 1.1$ (we justify this choice in Section 3.2 below). We show the resulting simulated image in Fig. 3. The image looks very similar to the real VLBI image in Fig. 2, in particular in also having enhanced brightness to the E and W.

While the real image has brightness contrasts of ∼2.2:1 between the hotspots to the east and west and the corresponding 'gaps' to the north and south, the simulated one with $\mathcal{R}_{\rm o/i} = 1.1$ had brightness contrasts of 1.4:1, which would increase if smaller values of $\mathcal{R}_{\rm o/i}$ were used for the model. This suggests that a significant part of the brightness enhancement to the east and west in our image is due merely to our elongated beam, although there may also be some real enhancement particularly to the east, where the observed image has higher brightness.

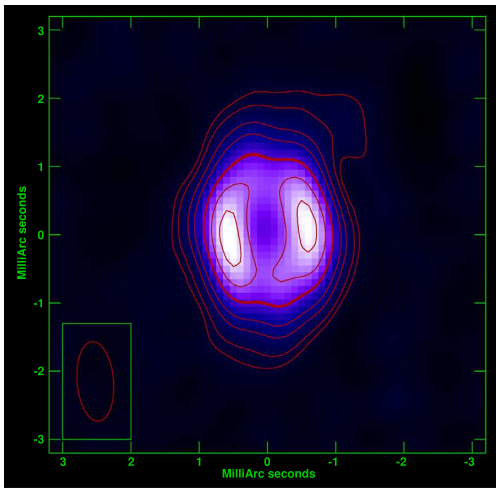

Figure 3. An image made by deconvolving model visibility data, where the u–v plane model was a completely spherically symmetrical shell. Random noise was added to the model visibilities to match the observed image. The deconvolution was the same as was used for the observed image. The model had outer angular radius, $\theta_{\rm o} = 0.89$ mas and $\mathcal{R}_{\rm o/i} = 1.1$. Despite being completely symmetrical, when convolved with the elliptical beam, the model image shows two hotspots very similar to those in the observed image (Fig. 2).

Our simulated data differ from the real measurements in one respect. Although we scaled the noise added to the simulated visibilities to produce the same image background rms, the noise we added was uncorrelated between visibilities. The real visibilities, on the other hand, are corrupted both by random and uncorrelated noise and by residual calibration errors. Since the calibration is antenna-based, this introduces correlations in the visibility errors for the real data not present in the simulated data. Since we phase self-calibrated, the residual calibration errors should be small, and it seems unlikely that such correlated errors would cause systematic changes in the apparent image morphology.

3.2 Size and expansion speed

To determine a precise size for SN 2014C, we fit a geometrical, spherical-shell model in the Fourier transform or u–v plane, as we did in Paper I.[4]

We used the same model we used in Paper I, which is the Fourier transform of the projection of an optically thin shell of emission. The model is characterized by the inner and outer angular radii of the shell, $\theta_{\rm i}$, $\theta_{\rm o}$, and the total flux density. We again used the square root of the data weights in the fitting, which makes the results more robust at the expense of some statistical efficiency.

We justify this choice of model geometry for SN 2014C in Paper I, and the same geometry has been found appropriate for other SNe (e.g. Bartel et al. 2002; de Witt et al. 2016). It is the outer angular radius, $\theta_{\rm o}$, which is most closely identified with the forward shock, and which is also most reliably determined by the data. We therefore first fix the ratio of $\mathcal{R}_{\rm o/i}$ ($= \theta_{\rm o}/\theta_{\rm i}$) to 1.25, which has been shown to be appropriate in the case of SN 1993J (Bietenholz et al. 2003; Bartel et al. 2007). For the case of a simple CSM structure and a non-magnetic shell, similar values were also seen in numerical

[4]Bietenholz et al. (2010a) showed that in the case of SN 1993J, the results obtained through u–v plane model fitting are superior to those obtained in the image plane.

simulations (Jun & Norman 1996). The fitted value of θ_o is only weakly dependent on the assumed value of $\mathcal{R}_{o/i}$.

As we found for earlier epochs, the purely statistical uncertainty on θ_o was small, ∼0.6 per cent. We follow the same procedure as in Paper I to estimate a systematic uncertainty, and again include three contributions in our final standard error, added in quadrature.

The first contribution was estimated using jackknife re-sampling (McIntosh 2016). Specifically, we dropped the data from each of the antennas in the VLBI array in turn and calculated $N_{antenna} = 12$ new estimates of the fitted size, and the scatter over these 12 values allows one to estimate the uncertainty of the original value that included all antennas. We obtained a jackknife relative uncertainty of 6.5 per cent.

The second contribution is an estimate of the effect of any residual mis-calibration of the antenna amplitude gains on the fitted sizes. We estimated this contribution to the uncertainty in a Monte Carlo fashion by repeatedly randomly varying the individual antenna gains by 10 per cent (rms), and then re-fitting the spherical shell models. This estimate should be conservative as it is unlikely that our antenna gains would be wrong by as much as 10 per cent. We find this causes a 1.4 per cent uncertainty in the fitted radius. The fitted angular outer radius with the full uncertainty is then $\theta_o = 0.94 \pm 0.06$ mas, with the assumption of $\mathcal{R}_{o/i} = 1.25$.

The fitted value of θ_o does depend weakly on $\mathcal{R}_{o/i}$. Therefore, rather than assuming $\mathcal{R}_{o/i} = 1.25$, we attempted to fit $\mathcal{R}_{o/i}$ in addition to θ_o. The result suggests a thin shell, with the best-fitting value being $\mathcal{R}_{o/i} = 1$, and a corresponding best-fitting $\theta_o = 0.85$ mas, about 0.09 mas, or 1.3σ smaller than the value obtained with the assumption of $\mathcal{R}_{o/i} = 1.25$.

The assumption of a completely optically-thin shell is likely not warranted as the unshocked ejecta are expected to remain optically thick to radio waves for decades (Mioduszewski, Dwarkadas & Ball 2001; Bietenholz & Bartel 2017). This will affect the fitted value of $\mathcal{R}_{o/i}$, in the sense that use of a completely optically-thin model will cause $\mathcal{R}_{o/i}$ to be overestimated. This is likely the reason why our best-fitting value of $\mathcal{R}_{o/i}$ is near unity, the maximum possible value, and the true value is likely to be lower.

An uncertainty on $\mathcal{R}_{o/i}$ is difficult to estimate. By definition, $\mathcal{R}_{o/i}$ cannot be <1, so any error in the estimate cannot be Gaussian-distributed. Since our FWHM resolution, even in the more well-resolved east–west direction, is only 0.54 mas, reliably determining the shell thickness of $\lesssim 0.20$ mas seems a tall order. We therefore cannot precisely determine $\mathcal{R}_{o/i}$, but we can say that it is likely between 1 and 1.25, with smaller values, corresponding to thinner shells, being more probable.

As might be expected, the inferred value of the outer radius, θ_o, is only very weakly dependent on absorption in the centre. In the case of SN 1993J, Bietenholz et al. (2003) fitted more elaborate models, which allowed for absorption in the centre of the SN and found almost no effect on the fitted values of θ_o, so the shortcomings of our optically-thin model are unlikely to significantly affect our values of θ_o.

We then take our final value for θ_o to be the mid-point of the two values obtained for $\mathcal{R}_{o/i}$ fixed at 1.25, and $\mathcal{R}_{o/i}$ free (with the fitted value $\mathcal{R}_{o/i} = 1$), and add in quadrature half the difference in those two values of θ_o to the uncertainty we had determined in the fixed $\mathcal{R}_{o/i} = 1.25$ case, to obtain a final value for θ_o of 0.89 ± 0.08 mas. At the distance of SN 2014C (15.1 Mpc), this radius corresponds to a linear size of $r_{16} = 20.1 \pm 1.7$.

3.3 Expansion curve

We plot our new value for the radius at $t = 4.8$ yr along with earlier ones from Paper I, in Fig. 4. The expansion of SNe is often

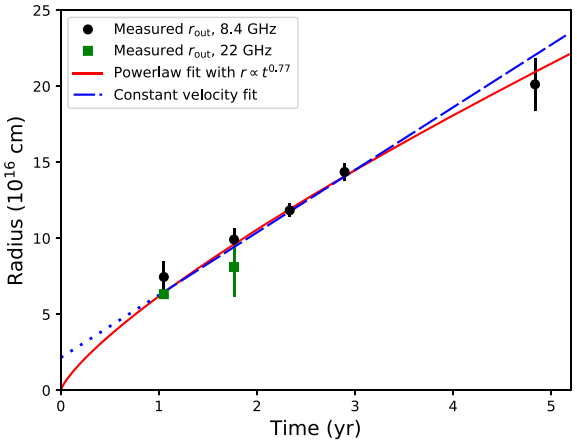

Figure 4. The radius of SN 2014C as a function of time, t, since the explosion at $t = 0$ on 2013 December 30. The outer radii were determined by fitting a spherical shell model directly to the visibilities in this paper and in Paper I, and calculated for a distance of $D = 15.1$ Mpc. Radii measured at 8.4 GHz are shown as black circles and those at 22 GHz as green squares. We show two different functions fitted to the measured radii. The first, shown by the solid (red) line, is an uninterrupted power-law expansion of the form $r \propto t^{m=0.77}$. The second, shown by the dashed (blue) line, is a constant velocity expansion after $t = 1$ yr (with an implied more rapid expansion before then). We expect the approximately constant-velocity regime to begin at $t \sim 1$ yr; hence, we show the extrapolation of the constant velocity fit to earlier times with a dotted line.

parametrized as a power law, such that $r = r_{1yr}(t / \mathrm{yr})^m$, where r is the radius of the SN at time t, r_{1yr} is the radius at $t = 1$ yr, and m is the power-law coefficient, often called the expansion parameter. Such a function has been shown to be expected on theoretical grounds with m in the range 0.6–1 (e.g. Chevalier 1982b), and used to describe other SNe (e.g. SN 1993J; Bartel et al. 2002).

The velocity between our previous measurement of r at $t = 2.9$ yr (Paper I) and the present one at $t = 4.8$ yr is 9400 ± 2900 km s^{-1}. If we interpret the evolution as a power law, the values at $t = 2.9$ and 4.8 yr imply $m = 0.66 \pm 0.18$, suggesting that, compared to the average velocity since the explosion, there is a moderate amount of deceleration over the last two measurements.

We turn now to fitting all the radius measurements. We fit the same two functions we used in Paper I to our measurements of r_{16} by least squares, and we refer the reader to that paper for a fuller discussion of the choice of functions. The first function is the power-law function just described.

Fitting a power-law function to our radius measurements, we obtain

$$r_{16} = (6.27 \pm 0.22) \times \left(\frac{t}{1\,\mathrm{yr}}\right)^{(0.77\pm0.03)} \left(\frac{D}{15.1\,\mathrm{Mpc}}\right),$$

with a sum of squared residuals, SSR = 2.4. We plot this fitted expansion curve as the red line in Fig. 4. The fitted value m is higher, albeit not significantly so, than that of $m = 0.66 \pm 0.18$ obtained from only the last two measurements, suggesting a possible increase in deceleration at the latest times.

The fitted expansion curve, with $m = 0.77$, suggests a moderate amount of deceleration over the history of the SN. This value of m is consistent with what is generally expected from the mini-shell model. If the CSM has a wind density profile ($\rho \propto r^{-2}$), then the mini-shell solution has that $m = (n - 3)/(n - 2)$ (Chevalier 1982b),

so our value of m suggests ejecta with $\rho \propto r^{-n}$ with a relatively flat value of $n = 6.5^{+0.8}_{-0.6}$.

In the self-similar solution of Chevalier (1982a), the value of $\mathcal{R}_{\rm o/i}$ depends on n, and for $n = 6.5$, a value of $\mathcal{R}_{\rm o/i} \simeq 1.3$ is expected, whereas our model-fitting suggested smaller values of $\mathcal{R}_{\rm o/i} \lesssim 1.25$ (Section 3.2). However, since the density structure of SN 2014C's CSM was clearly more complex than a simple $\rho \propto r^{-2}$ power law assumed in the self-similar model, we should expect that the relationships between m, n, and $\mathcal{R}_{\rm o/i}$ will deviate somewhat from those in the self-similar case.

There are, however, good reasons to think that a simple power law may not be appropriate to describe SN 2014C's expansion. As we described in the introduction, at about $t \sim 0.3$ yr, SN 2014C's expanding shock seems to have encountered a region of dense, H-rich CSM, leading to an evolution that deviates from the self-similar power-law function of the mini-shell model. Systems of this nature have been considered by numerous authors (Chevalier & Liang 1989; Chugai & Chevalier 2006; Smith & McCray 2007; van Marle et al. 2010). In such a system, the shock slows dramatically when it first encounters the dense shell. It then accelerates as it emerges from the dense CSM shell, and subsequently proceeds to coast at almost constant speed until the mass of the CSM swept up from outside the massive shell becomes comparable to the shell mass, at which point an approximately power-law expansion resumes. This behaviour has been reproduced in numerical simulations by van Marle et al. (2010).

The impact of the SN shock on the dense CSM shell for SN 2014C occurred at $t \sim 0.3$ yr, before the first VLBI observations at $t = 1.1$ yr. We cannot, therefore, directly resolve the slowing of the shock, so we model only the period of approximately constant-velocity expansion after the impact of the shock on the massive shell. Hence, the second function that we fit to SN 2014C's expansion, which we call the 'constant velocity' function, is $r[t > t_{\rm impact}] = r_{\rm impact} + v_{\rm post}\ (t - t_{\rm impact})$, where $t_{\rm impact}$ is the time at which the shock impacts on the dense shell, $r_{\rm impact}$ is the radius at that time, and $v_{\rm post}$ is the shock velocity after that time. For $t_{\rm impact} \leq 1$ yr, that function is equal to $r = r_{\rm 1yr} + v_{\rm post} \cdot (t - 1\,{\rm yr})$, so we fit the latter function and avoid the problem of not knowing $t_{\rm impact}$ exactly. It is expected that $t_{\rm impact}$ is in the range $0.3 \sim 0.6$ yr (e.g. Harris & Nugent 2020). We again fit the function to the VLBI radius measurements using weighted least squares.

Note that the power-law function also produces constant-velocity expansion when $m = 1$, but there is a crucial difference between the two functions: the power-law function with $m = 1$ is just uninterrupted free expansion starting from $r = 0$, $t = 0$, whereas our constant velocity function only has a constant velocity after $t = 1$ yr, and does not extrapolate to $r = 0$, $t = 0$, since a more rapid expansion at $t < 1$ yr is implicit.

Fitting the constant-velocity function, we obtained

$$r_{16} = (6.27 \pm 0.22) + (4.12 \pm 0.22) \times \left(\frac{t}{1\,{\rm yr}} - 1\right)\left(\frac{D}{15.1\,{\rm Mpc}}\right),$$

where the fitted radius at 1 yr is $(6.27 \pm 0.22) \times 10^{16}$ cm and the post-impact velocity is $v_{\rm post} = (4.12 \pm 0.22) \times 10^{16}$ cm yr^{-1}, or $13\,040 \pm 690$ km s^{-1}. The SSR of this fit was 3.7, and we plot the fitted function as the blue line in Fig. 4.

The SSR values for the power law and the constant velocity fitted functions were 2.4 and 3.7, respectively, and therefore our data do not distinguish reliably between the two, although the power-law function is a slightly better fit. The values of SSR are close to the most probable value for a χ^2 distribution with 5 degrees of freedom, $\chi^2_5 = 3$, indicating a reasonable fit, although we note that our measurement errors are likely correlated, so the SSR is likely not exactly χ^2-distributed. The slightly better fit of the power-law form may be due to the constant-velocity period having ended and the power-law expansion resuming, as is expected at late times after the impact of the ejecta on the CSM shell (Harris & Nugent 2020).

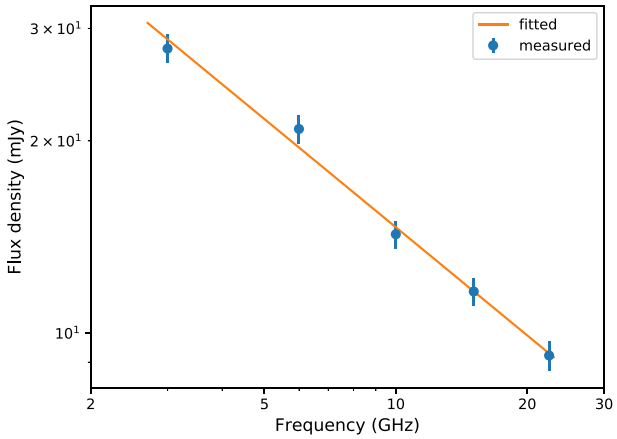

Figure 5. The SED of SN 2014C on 2020 May 6, at $t = 6.3$ yr. The plotted errorbars show 1σ standard errors, which include both systematic and statistical contributions, and the straight line shows the power-law spectrum fitted to the data, which has a spectral index $\alpha = -0.56 \pm 0.03$.

Table 1. VLA flux density measurements on 2020 May 6.

Frequency (GHz)	Flux density[a] (mJy)
3.0	27.9 ± 1.4
6.0	20.9 ± 1.1
10.0	14.3 ± 0.7
15.1	11.6 ± 0.6
22.4	9.8 ± 0.5

[a]Our standard errors include the image background rms values and a 5 per cent flux-density calibration error, added in quadrature.

3.4 VLA flux density measurements

On 2020 May 6, we measured the flux density of SN 2014C over a range of frequencies between 3.0 and 23 GHz. We show the SED in Fig. 5. A power law with spectral index, $\alpha = -0.56 \pm 0.03$, (where $S_\nu \propto \nu^\alpha$), and $S_{5\,\rm GHz} = 21.6 \pm 0.6$ mJy fits all the measurements to within the uncertainties, with the SSR (sum of squared residuals) being 2.4, which is close to the expectation value of χ^2_3.

We give the flux densities measured from our VLA observations in Table 1. We show the 4.9- and 7.1-GHz light curves in Fig. 6, where we also show for comparison the 15.7-GHz light curve measured by the Arcminute Microkelvin Imager from Anderson et al. (2017). The light curves do show the usual pattern of an earlier rise at higher frequencies. However, the overall nature of the light curve is quite unusual, with a slow rise till $t \sim 0.6$ yr that occurs in steps at least at 15 GHz, followed by a flat curve with an almost value for the almost 6 yr since $t \sim 1$ yr.

4 DISCUSSION

4.1 Morphology of SN 2014C

The new VLBI image of SN 2014C at $t = 4.8$ yr (Fig. 2) confirms the shell structure suggested by our earlier VLBI image from ∼2 yr earlier (Paper I). The source remains relatively circular in outline.

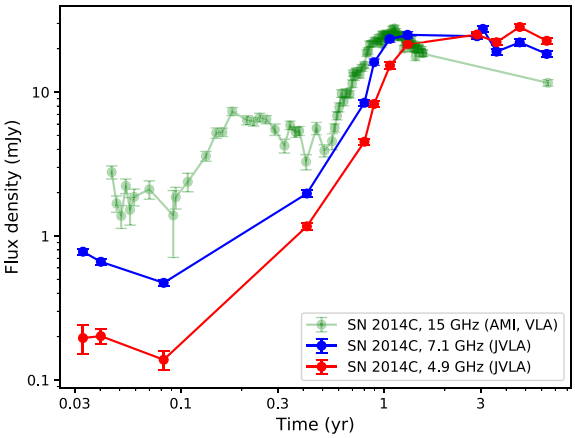

Figure 6. The radio light curves of SN 2014C at three frequencies. Red and blue show our VLA measurements at 4.9 and 7.1 GHz, respectively. Green shows the 15-GHz light curve, with all except the last point being at 15.7 GHz from AMI (Anderson et al. 2017), and the last point being our own VLA measurement at 15.1 GHz (Table 1). We plot 1σ standard errors with statistical and dominating 5 per cent systematic contributions added in quadrature. In many cases, the errorbars are smaller than the plotted points. The last pair of values at 4.9 and 7.1 GHz (at $t = 6.3$ yr) were interpolated between the measurements at 3.0 and 6.0, and 6.0 and 10.0 GHz, respectively.

Two enhancements in brightness are visible to the east and west. These are likely largely due to convolution of a ring-like pattern with an elliptical restoring beam, rather than being intrinsic brightness enhancements, fortuitously aligned with the restoring beam. In our tests with synthetic data, a completely circularly symmetric shell model produces an image very similar to the observed one when convolved with our elliptical restoring beam (see Section 3.1, Fig. 3).

Although a spherical shell structure is consistent with our VLBI image, could SN 2014C in fact have a different structure? Given the observed image (Fig. 2), is it possible that the source is intrinsically bipolar or elliptical, rather than having a spherical shell structure? Bi-polar jets occur in GRB and possibly in some SNe (e.g. Papish & Soker 2011). SN 1987A, on the other hand, has a structure that is axially, but not spherically symmetric (e.g. McCray & Fransson 2016).

To compare a possible bipolar structure to the spherical shell structure, whose projection on to the sky plane is circularly symmetrical, we fitted a model consisting of two circular Gaussians to directly the visibilities in the same way we fitted the spherical shell model in Section 3.2. We found the fit considerably poorer, despite the two-Gaussian-component model having more free parameters. We can therefore say that the observations disfavour a simple bipolar structure.

A circular ring-like structure at some angle to the plane of the sky, similar to SN 1987A's equatorial ring, is harder to constrain in this manner, and if the ring is oriented near to the plane of the sky the projected image will strongly resemble the projection of a thin spherical shell. A tilted ring structure of this nature could therefore be also compatible with the VLBI image. Future VLBI observations at higher relative resolution may allow us to more definitely determine the emission geometry.

4.2 Radius and expansion speed

From our VLBI measurements, we determined the radius of the radio emission region, which probably corresponds to the radius of the forward shock (see Bartel et al. 2007, for a discussion on the relationship between the radio emission region and the forward shock in the case of SN 1993J). At $t = 4.8$ yr, we measured a radius of $r_{16} = 20.5 \pm 1.8$ (for $D = 15.1$ Mpc). The velocity between our previous measurement at $t = 2.9$ yr (Paper I) and the present one is 9400 ± 2900 km s^{-1}.

This velocity is consistent within the uncertainties, but lower by 0.8σ, than the value of $14\,000 \pm 4200$ km s^{-1} we found between $t = 2.3$ and 2.9 yr (Paper I), suggesting that the shock front is likely decelerating somewhat.

We found in Section 3.3 that a power-law model fits all the VLBI radius measurements marginally better than a constant velocity model (see Fig. 4). Our latest radius measurement ($t = 4.8$ yr) suggests a possible increase in the deceleration at the latest times, in either the constant-velocity or the power-law models of the expansion. Further VLBI measurements should be undertaken to better constrain any change in deceleration.

Given the complicated nature of SN 2014C's CSM, with, going outward, first a low-density cavity, then a very dense shell, then a moderately dense stellar wind, the real expansion curve will be more complex than a simple power law. In Paper I, we compared the evolution of SN 2014C to scaled hydrodynamic simulations from van Marle et al. (2010) to show the generally expected behaviour of an SN shock slowing down dramatically upon first encountering a thick shell, but the shock speed then recovering somewhat.

Since then, Harris & Nugent (2020) have performed new hydrodynamic simulations more specifically aimed at cases like SN 2014C. They find the measurements can be accounted for with the following model: SN 2014C explodes in a low-density cavity. The ejecta first impact on the dense CSM shell at $t \sim 0.3$ yr (100 d), then exit the dense shell again at $t \sim 0.5$ yr (190 d), subsequently interact with a wind medium with $\rho \propto r^{-2}$ corresponding to a period before the ejection of the dense shell, where the progenitor was loosing mass relatively steadily. This model is also consistent with the VLBI radius measurements; however, as we show in Section 4.4, the radio light curves suggest a slight variation.

4.3 Spectral energy distribution

We found that the spectrum of the radio emission at $t = 6.3$ yr was well described by a power-law spectrum, with $S_\nu = (21.6 \pm 0.6$ mJy$) \times (\nu/(5\,\mathrm{GHz})^\alpha$ with $\alpha = -0.56 \pm 0.03$. Such a spectrum is what is expected from optically-thin emission resulting from the SN shock, although α is somewhat flatter than usual: Weiler et al. (2002) fitted the optically-thin values of α for 14 different SNe, and our value for SN 2014C is close to their flattest value of $\alpha = -0.55$ (which was for the SN IIL, SN 1970G).

The relatively flat spectrum of SN 2014C might just be due to a slow transition from optically-thick (inverted spectrum) to optically-thin. As can be seen from the 4.9- and 7.1-GHz light curves in Fig. 6, the spectrum between these two frequencies remained inverted until $t \sim 3$ yr. If the spectrum were still transitioning between optically thick and thin, one would expect significant curvature in the spectrum, with a steep spectrum at high frequencies and a flat (or inverted one) at low frequencies. Indeed, our lowest frequency measurement at 3 GHz suggests a marginally flatter spectrum below 6 GHz. If we fit only the points at 6 GHz and above, we obtain $\alpha = -0.61 \pm 0.04$, which is within the normal range.

Bartel et al. (2002) found also that the optically-thin value of α for the SN IIb, SN 1993J, became flatter with time. Maeda (2013) shows that such a flattening is in fact expected, with the shock acceleration being less efficient in young SNe where the shock speed is high, leading to steeper spectra, and becoming more efficient later on,

leading to flatter spectra for SN remnants, for which α clusters around the expected value for shock acceleration of $\alpha = -0.5$. This process may also be occurring in SN 2014C, and contributing to the relatively flat value of α.

4.4 Radio light curve

From our VLA observations at $t = 6.3$ yr, we found that the light curve has an extended, almost constant, plateau since $t \sim 0.8$ yr. Such a light curve is unusual, the light curves of the majority of SNe show an approximately power-law decline after a time on the order of one month (e.g. Weiler et al. 2002; Bietenholz et al. 2020).

The strong and sustained radio emission is interpreted as being due to the strong CSM interaction as the forward shock ploughed through the dense CSM shell. The rate of particle acceleration is dependent on the CSM density but is also strongly dependent on the shock velocity. Harris & Nugent (2020) show that while the CSM density drops when the shock emerges from the dense shell, the shock speed increases, which can lead to an increase in radio emission despite the drop in CSM density.

However, these increases in the shock velocity are temporary, and since the shock emerged from the dense shell some time ago, why is the radio brightness still staying high? In the self-similar mini-shell model of an SN, where both the ejecta and the CSM density structures are power laws in radius, the radio brightness evolves as $S \propto t^{\beta}$ (Fransson, Lundqvist & Chevalier 1996), with

$$\beta = -\{3 - \alpha - [6 - \alpha - (s/2)(3 - \alpha)][(n - 3)/(n - s)]\},$$

where the density of the CSM is $\propto r^{-s}$, that of the ejecta is $\propto r^{-n}$, and α is the radio spectral index. Although in the case of SN 2014C, it is clear that the CSM structure is more complex than a simple power law, and strictly self-similar evolution is therefore not expected, it is none the less instructive to compare SN 2014C's evolution to expectations from the self-similar case. It is expected that at some point after the shock has passed through the dense CSM, the evolution would once again approach being self-similar. Since the radio brightness of SN 2014C has not declined much, $\beta \simeq 0$. For a typical value of $n = 16$ and our observed $\alpha = -0.56$, in a self-similar scenario, we would have $s = 1.45$. Since SN 2014C's evolution was not self-similar, the actual value of s will probably differ. However, the shock exited the dense CSM shell already at $t \sim 0.3$ yr, so by $t \sim 6.3$ yr probably SN 2014C's evolution is again approaching the self-similar solution, and that value of s at least approximately correct. The flat light curve therefore probably suggests a CSM density profile notably flatter than that for a steady wind (density $\propto r^{-2}$). The exact value of n has only a minor effect on this conclusion, which holds for any reasonable value of n.

Harris & Nugent (2020) suggest that SN 2014C's shock crossed through a dense shell of CSM, and is now interacting with a wind CSM, with $s = 2$. While this scenario fits the measured sizes and expansion velocities, it is hard to reconcile with the lack of any decay in the radio luminosity. The flat light curve suggests $s \sim 1.5$, implying that the shock is currently interacting with CSM from a period where the progenitor's mass-loss was relatively steadily decreasing with time. Harris & Nugent (2020) found that both models with $s = 2$ (a steady wind) and $s = 1$ (wind with density decreasing with time) were compatible with the measurements, therefore a model with $s = 1.5$ should also be compatible with the data.

The decrease in time of the mass-loss rate of the progenitor must have occurred only over a bounded period, and there was likely steadier mass-loss rate before the decrease. The shock radius is currently 2.05×10^{17} cm. If we assume a wind speed of 1000 km s^{-1}, typical of a Wolf–Rayet like progenitors, the shock is currently interacting with material lost from the star only about a century before the explosion. Even if the wind speed was 10 km s^{-1}, typical of supergiants, the age of the material is only of order 10^4 yr. Fluctuations in the mass-loss rate over these time-scales, short compared to the age of the star, have been seen or inferred in a number of stars (e.g. Smith 2014). It is likely, therefore, that the light curve will turn over and decrease in the future as the shock moves beyond the region formed by the mass-loss that was declining in time prior to the massive shell ejection shortly before the explosion.

5 SUMMARY AND CONCLUSIONS

We report on our new VLBI and VLA observations of SN 2014C. We resolved the radio emission from the expanding shell of ejecta and determined the radius of the emission region at $t = 4.8$ yr after the explosion. Comparing these results with those of our earlier VLBI measurements, we found the following:

(1) Our new VLBI observations show a structure that is relatively circular in outline and enhanced towards the outer edge. There is a clear enhancement to the east and west, much of which is likely not intrinsic, but rather due to the convolution with an elongated restoring beam. Some intrinsic enhancement of the surface brightness does however seem likely, particularly to the east. The observed image is compatible with a relatively thin spherical shell seen in projection. Our model fits show that a simple bipolar structure is unlikely. A ring-like structure, however, could also be compatible with the image.

(2) At $t = 4.8$ yr, the angular outer radius of the SN was 0.91 ± 0.08 mas, corresponding to $(20.5 \pm 1.8) \times 10^{16}$ cm (for a distance of 15.1 Mpc). The speed between the last two epochs of VLBI observations ($t = 2.9$ and 4.8 yr) was 9400 ± 2900 km s^{-1}.

(3) The expansion of SN 2014C, as determined from VLBI observations ($t = 1.1$–4.8 yr) is compatible with power-law expansion, with $r \propto t^{0.77 \pm 0.03}$, suggesting a moderate amount of deceleration over the SN's lifetime. The measurements are compatible with an early deceleration, and an approximately constant-velocity expansion with $13\,040 \pm 690$ km s^{-1} since $t = 1.1$ yr. There is a suggestion that the deceleration is increasing again after $t \sim 3$ yr.

(4) The radio spectral energy distribution is consistent with a power law with $S \propto \nu^{\alpha}$ where $\alpha = -0.56 \pm 0.03$. This value of α is somewhat flatter than that seen in the majority of SNe. There is a hint of flattening of the spectrum below 6 GHz, as might be expected if it were just now becoming optically thin at low frequencies.

(5) The radio light curve at $\sim$6 GHz had reached a peak of $\sim$25 mJy, corresponding to a νL_{ν} luminosity of 4.1×10^{37} erg s^{-1}, after about 1 yr, and has stayed almost constant since then, up to our latest measurement at $t = 6.3$ yr.

(6) Our observations are consistent with a picture that has emerged of SN 2014C having a mass-loss event that ejected a very dense shell not long before the explosion, with the mass-loss rate prior to the shell ejection being much lower.

(7) The sustained radio emission since $t \sim 1$ yr suggests that the progenitor went through a period of steadily decreasing mass-loss before ejecting the dense shell and then exploding as an SN.

ACKNOWLEDGEMENTS

We thank the teams of both the EVN and the VLA for their work to make the observations possible. The EVN is a joint facility of independent European, African, Asian, and North American radio astronomy institutes. The National Radio Astronomy Observatory

is a facility of the National Science Foundation operated under cooperative agreement by Associated Universities, Inc. We have made use of NASA's Astrophysics Data System Abstract Service. This research was supported by both the National Sciences and Engineering Research Council of Canada and the National Research Foundation of South Africa.

We also thank the anonymous referee for his or her comments that improved this paper.

DATA AVAILABILITY STATEMENT

The raw data underlying this paper are available in EVN and NRAO archives, and can found under the observing codes EB066A, EB066B for the EVN and 20A-441 for NRAO. The calibrated data or images underlying this paper will be shared on reasonable request to the corresponding author.

REFERENCES

Anderson G. E. et al., 2017, MNRAS, 466, 3648
Bartel N. et al., 2002, ApJ, 581, 404
Bartel N., Bietenholz M. F., Rupen M. P., Dwarkadas V. V., 2007, ApJ, 668, 924
Bartel N., Karimi B., Bietenholz M. F., 2017, Astron. Rep., 61, 299
Bietenholz M. et al., 2010a, 10th European VLBI Network Symposium and EVN Users Meeting: VLBI and the New Generation of Radio Arrays, SISSA, Trieste (Italy)
Bietenholz M., 2014, 12th European VLBI Network Symposium and Users Meeting, SISSA, Triete
Bietenholz M. F., Bartel N., 2017, ApJ, 851, 124
Bietenholz M. F., Bartel N., Rupen M. P., 2003, ApJ, 597, 374
Bietenholz M. F., Bartel N., Milisavljevic D., Fesen R. A., Challis P., Kirshner R. P., 2010b, MNRAS, 409, 1594
Bietenholz M. F., Kamble A., Margutti R., Milisavljevic D., Soderberg A., 2018, MNRAS, 475, 1756 (Paper I)
Bietenholz M. F., Bartel N., Argo M., Dua R., Ryder S., Soderberg A., 2020, ApJ, preprint (arXiv:2011.11737)
Chevalier R. A., 1982a, ApJ, 258, 790
Chevalier R. A., 1982b, ApJ, 259, 302
Chevalier R. A., Fransson C., 2017, in Alsabti A. W., Murdin P., eds, Handbook of Supernovae, Thermal and Non-thermal Emission from Circumstellar Interaction, Springer International Publishing, 875
Chevalier R. A., Liang E. P., 1989, ApJ, 344, 332
Chugai N. N., Chevalier R. A., 2006, ApJ, 641, 1051
de Witt A., Bietenholz M. F., Kamble A., Soderberg A. M., Brunthaler A., Zauderer B., Bartel N., Rupen M. P., 2016, MNRAS, 455, 511
Fransson C., Lundqvist P., Chevalier R. A., 1996, ApJ, 461, 993
Harris C. E., Nugent P. E., 2020, ApJ, 894, 122
Hunter D. A. et al., 2012, AJ, 144, 134
Jin R., Kong A. K. H., 2019, ApJ, 879, 112
Jun B., Norman M. L., 1996, ApJ, 465, 800
Kamble A., Soderberg A., Zauderer B. A., Chakraborti S., Margutti R., Milisavljevic D., 2014, Astron. Telegram, 5763
Keimpema A. et al., 2015, Exp. Astron., 39, 259
Kim M. et al., 2014, Cent. Bur. Electr. Telegrams, 3777
McCray R., Fransson C., 2016, ARA&A, 54, 19
McIntosh A., 2016, preprint (arXiv:1606.00497)
McMullin J. P., Waters B., Schiebel D., Young W., Golap K., 2007, in Shaw R. A., Hill F., Bell D. J., eds, ASP Conf. Ser. Vol. 376, Astronomical Data Analysis Software and Systems XVI. Astron. Soc. Pac., San Francisco, p. 127
Maeda K., 2013, ApJ, 762, L24
Margutti R. et al., 2017, ApJ, 835, 140
Milisavljevic D. et al., 2015, ApJ, 815, 120
Mioduszewski A. J., Dwarkadas V. V., Ball L., 2001, ApJ, 562, 869
Papish O., Soker N., 2011, MNRAS, 416, 1697
Rich J. W., de Blok W. J. G., Cornwell T. J., Brinks E., Walter F., Bagetakos I., Kennicutt R. C., Jr., 2008, AJ, 136, 2897
Saha A., Thim F., Tammann G. A., Reindl B., Sandage A., 2006, ApJS, 165, 108
Smith N., 2014, ARA&A, 52, 487
Smith N., McCray R., 2007, ApJ, 671, L17
Tartaglia L., Pastorello A., Benetti S., Cappellaro E., Tomasella L., Ochner P., Elias-Rosa N., Turatto M., 2014, Astron. Telegram, 5742
Tinyanont S. et al., 2019, ApJ, 887, 75
van Marle A. J., Smith N., Owocki S. P., van Veelen B., 2010, MNRAS, 407, 2305
Wakker B. P., Schwarz U. J., 1988, A&A, 200, 312
Weiler K. W., Panagia N., Montes M. J., Sramek R. A., 2002, ARA&A, 40, 387
Zauderer B. A., Kamble A., Chakraborti S., Soderberg A., 2014, Astron. Telegram, 5764

This paper has been typeset from a TEX/LATEX file prepared by the author.